Mechanical properties and in-situ deformation imaging of micro-lattices manufactured by laser based powder bed fusion

Anton Du Plessis [1,*], **Dean-Paul Kouprianoff** [2], **Ina Yadroitsava** [2] **and Igor Yadroitsev** [2]

[1] CT Scanner Facility, Stellenbosch University, Stellenbosch, South Africa 7602
[2] Department of Mechanical Engineering, Central University of Technology, Free State, Bloemfontein, South Africa 9300
* Correspondence: anton2@sun.ac.za; Tel.: +27-21-808-9389

Abstract: This paper reports on the production and mechanical properties of Ti6Al4V micro-lattice structures; with strut thickness nearing the single-track width of the laser-based powder bed fusion (LPBF) system used. Besides providing new information on the mechanical properties and manufacturability of such thin-strut lattices; this paper also reports on the in-situ deformation imaging of micro-lattice structures with 6 unit cells in every direction. LPBF lattices are of interest for medical implants; due to the possibility of creating structures with an elastic modulus close to that of the bones and small pore sizes which allow effective osseointegration. In this work four different cubes were produced by laser powder bed fusion and subsequently analyzed using microCT; compression testing and one selected lattice was subjected to in-situ microCT imaging during compression. The in-situ imaging was performed at 4 steps during yielding. The results indicate that mechanical performance (elastic modulus and strength) correlate well with actual density and that this performance is remarkably good; despite the high roughness and irregularity of the struts at this scale. In-situ yielding is visually illustrated.

Keywords: laser powder bed fusion; additive manufacturing; X-ray tomography; in-situ imaging; Ti6Al4V; lattice structures

1. Introduction

Additive manufacturing (AM) is an emerging production technique whereby a part with complex geometry can be produced directly from a design file in a layer-by-layer method [1], [2]. In the case of laser based powder bed fusion (LPBF), a single layer of the part is selectively fused using a laser beam which is scanned across a powder bed surface in a series of tracks, new powder is delivered and the next layer is scanned and fused. Predictably the part integrity requires that single tracks are stable [3] and well overlapped with one another as well as layers to prevent unwanted porosity in solid parts. This has been discussed in some detail in a recent review of the use of X-ray microtomography in additive manufacturing [4]. Despite the possibility of irregularities in parts, it is possible to produce parts with excellent mechanical properties when process parameters are optimized, see for example [5] for biomedical Ti6Al4V produced by LPBF.

One of the major benefits brought about by additive manufacturing is the ability to produce complex parts, and this is especially true for lattice structures which are regularly spaced and repeating combinations of struts with spaces between them. Lattice structures produced by AM have been the topic of many studies in recent years due to the potential to use these in bone replacement implants [6]–[8]. In implants, the porous nature of the lattice structure is beneficial to lower the elastic modulus of biocompatible materials to match that of the bone at the implant interface, minimizing the possibility for stress shielding causing loss in bone density in the vicinity. Additionally, the open

45 porous nature allows for bone ingrowth into the lattice, effectively ensuring a good bond with the
46 existing bone.
47   The investigation of the mechanical properties of lattices produced by AM and in particular
48 LPBF is therefore crucial for the adoption of this type of design in implants, along with tailoring its
49 properties for the application of custom shapes which meet local bone density requirements. In
50 general the mechanical properties of these structures can be predicted by the Ashby-Gibson model
51 for open-cell foams [9], [10], with a general relationship for elastic modulus of the lattice (E) as a
52 function of the lattice density (ϱ) and elastic modulus of the solid material used (E_s), given as follows:

$$E = \propto_2 E_s \left(\frac{\rho}{\rho_S}\right)^2$$

54 Where $\propto_2$ is a value between 0.1 and 4 depending on the lattice geometry [9].

55   In early work by Parthasarathy et al [11], simple cubic lattices of Ti6Al4V produced by electron
56 beam melting where analyzed by microCT and mechanical testing and it was found that the
57 mechanical properties are weaker than predicted and this was especially so for a model with thinner
58 struts. This might be attributed to manufacturing irregularities such as the rough as-built surface and
59 unexpected porosity inside struts. Geometric accuracy is often a limitation in additive manufacturing
60 of cellular structures, as is the entrapment of powder in the small pore spaces of these structures [1].
61 Various LPBF cellular structures in Ti6Al4V have been produced in different unit cell designs and
62 their mechanical properties investigated, for example cubic [12], diamond [13], combinations of
63 designs including body-centred cubic [14] and minimal surfaces [15]. Besides variations in
64 mechanical performance induced by geometric inaccuracy and manufacturing errors, slight
65 variations also exist in the properties of various lattice designs themselves. This was demonstrated
66 recently by the numerical analysis of various lattice designs, ignoring manufacturing imperfections
67 [16].
68   It is therefore clear that the only way to fully understand the complex behavior of lattice
69 structures (with many variations in designs and varying amounts of manufacturing errors, which to
70 some extent also depend on the design), is to use high resolution imaging. In prior work, using
71 relatively large lattices with struts more than 1 mm in diameter, compression tests combined with
72 microCT imaging was used to visualize the first yielding crack locations as shown in [17], with loads
73 up to 140 kN. This was done ex-situ by stopping the mechanical test at first yielding and correlating
74 "before" and "after" microCT scans to find cracks / yielding locations. Some work has also previously
75 been done using in-situ synchrotron tomography during loading of small unit cells produced by
76 LPBF [18]. This work showed local strut-scale deformations during yielding and compared
77 experimental results to those predicted by simulation, but was limited to unit cells which are not
78 necessarily representative of tessellated lattices.
79   In this work the aim was to investigate the smallest possible lattices that can be produced with
80 a typical LPBF system with track width of roughly 0.1 mm. In addition to investigating the
81 mechanical properties of such small lattices, the accuracy of these produced micro-lattices may be
82 useful as a reference for future work. Four different sizes of lattice cube samples were produced, each
83 containing 6 unit cells in each direction with a diamond unit cell design with porosity of 80% and
84 unit cell sizes 0.6, 0.8, 1.0 and 1.2 mm. Since the geometry and the density is kept constant, the
85 theoretical elastic modulus and yield stress should be identical in all four cases, therefore the aim was
86 to investigate the properties as the struts become thinner with decreasing unit cell size. The
87 mechanical properties of these small lattices is reported and in-situ imaging of the lattice deformation
88 using high resolution X-ray tomography is demonstrated.

2. Materials and Methods

Models were designed in Materialize Magics [19] and produced from Ti6Al4V ELI powder by EOSINT M 280 (EOS GmbH – Electro Optical Systems) with 200 W laser and original parameters Ti64_Performance 1.1.0 (30 µm). Gas atomized Ti6Al4V ELI powder from TLS Technik GmbH & Co. Spezialpulver KG was used. Particle size distribution was as follows: equivalent diameters (weighted by volume) d_{10}= 12.1 µm; d_{50}=23.6 µm; d_{90}=37.6 µm. Chemical composition fulfils the requirements of ASTM F136 (regarding maximum concentration of impurities).

A stress-relief cycle for 3 hours at 650 C [5] was conducted in argon atmosphere after producing the parts, after which the parts were cut from the build plate using electrical discharge machining. The unit cell design used in this work was the diamond design - the unit cell is shown in Figure 1(a). Three samples of each of 4 designs were produced – the computer aided design (CAD) designs are shown in Figure 1(b), with a strut thickness analysis showing that the larger the unit cell, the thicker is the strut as expected. Strut thickness analysis allows measurement of the "wall" thickness at every point in the structure. In this case the sphere-method was used, which provides the value of the maximal-fitted sphere in every point in the structure. The designs were selected to produce cubes with 6 unit cells in each direction, with unit cell sizes for the 4 designs being 0.6, 0.8, 1.0 and 1.2 mm. This ensures that the density is kept constant and was selected to be 20% dense (80% porosity). The physical sample sizes varied from 3.6 mm to 7.2 mm for the lattice region, and additional solid material was added to the top and bottom to make the total height 8 mm in all cases, for simpler loading in the compression cell.

(a)

(b)
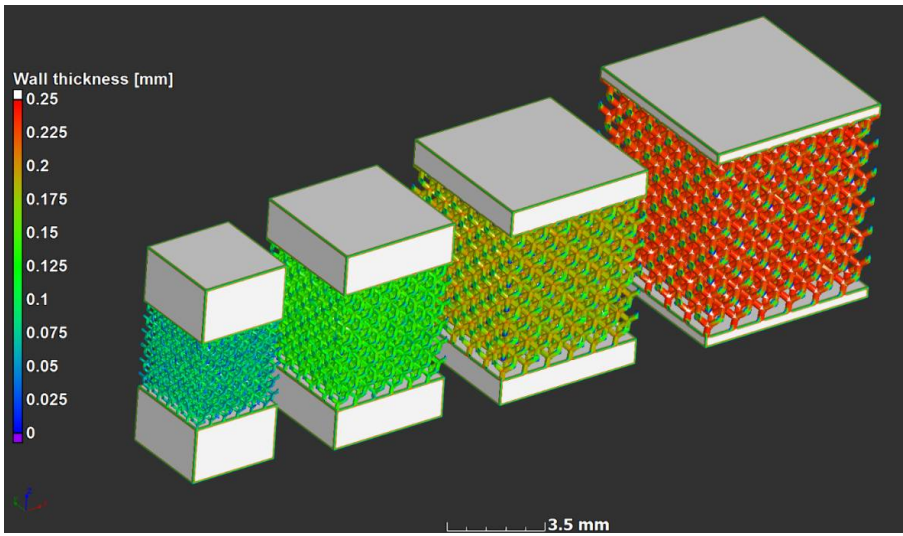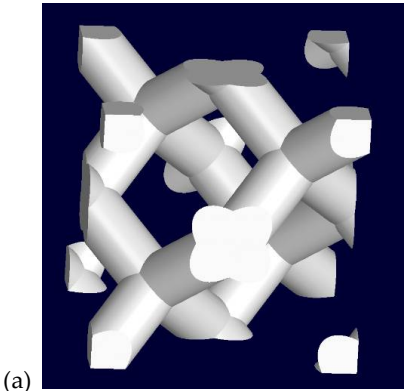
Figure 1. Design of microlattices showing (a) a single unit cell design – diamond type, and (b) the four full CAD lattice design used – unit cell sizes 0.6, 0.8, 1.0 and 1.2 mm, with strut thickness analysis.

120   MicroCT scanning was done using laboratory nanoCT as described in [20] using a Deben in-situ
121 loading stage (CT500) in a General Electric Nanotom scanner. The sample sizes in this work were
122 selected according to the maximum sample size of 10 mm and maximum loading force of 500 N of
123 this loading stage. One sample design which did not fail up to 500 N was additionally subjected to
124 compression tests on a different loading stage to obtain the yield strength. This was the smallest
125 sample with highest density (Figure 1, sample on the far left).
126   MicroCT voxel size was selected as 4 μm, with 140 kV and 130 μA for X-ray generation, using
127 0.5 mm copper beam filtration and using continuous scanning mode, a total of 3600 images were
128 recorded during a full rotation of the sample. Images were further analyzed in Volume Graphics
129 VGSTUDIO MAX 3.2 [21]. Wall thickness analysis used in this work was done with the sphere-
130 method. Due to file sizes and limited computing power, the combined images were resampled in
131 VGSTUDIO MAX to 10 μm voxel size and 8 bit data depth to reduce file sizes and memory usage
132 and ease the image analysis.
133

3. Results and discussion

135   Samples were manufactured successfully, but microCT analyses show that the strut thickness
136 across the models did not vary as expected – this is shown in Figure 2 using a strut thickness analysis,
137 analogous to Figure 1. Irregularities are expected at this scale due to various practical limitations
138 which exist when producing small intricate parts during LPBF. The cause of such irregularities can
139 be explained when looking at the minimum size of the designed features with regard to the
140 combined effects of laser spot size, building direction, layer thickness and the implemented scanning
141 strategy for core, overhangs and top surfaces; all having an effect on the amount of detail that can be
142 obtained. Small features are also governed by the single track's width and attached powder particles
143 which in turn are limited by powder particle size distribution. Accuracy of small overhangs is not
144 only dependent on the layer thickness but also on the loose powder and the inability of the molten
145 pool to penetrate into solid material of the lattice. Therefore irregular surfaces below the struts are
146 expected [22].
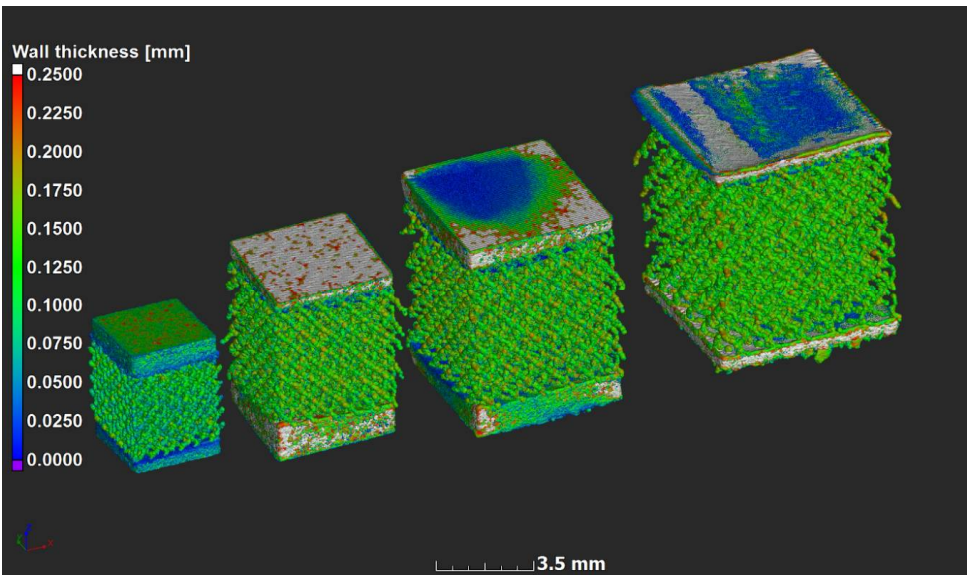
Figure 2. MicroCT scan data 3D rendering with strut thickness colour coding on the micro-lattices. Models with a 0.6, 0.8, 1.0 and 1.2 mm unit cell size from left to right respectively – here the top and bottom of the samples were slightly cropped as the lattice area was scanned only. Dark blue indicates thin local walls and red indicates thick walls, thickest parts excluded to highlight the important aspect: all lattice struts have similar thickness (0.1-0.15 mm).

153   In previous work [23] it was shown that at layer thickness 15-45 µm and similar Ti6Al4V powder
154   and process-parameters, the width of the track was 100-150 µm. The small size of the designed struts,
155   which are close to the single-track width of the laser melting track width, combined with the scanning
156   strategy of the LPBF system used apparently did not allow for variations and these lattices were
157   seemingly all produced with similar strut thickness deviating from the design thickness as shown in
158   Figures 3 (a) and 4. On the one hand, .stl triangulation of small structures leads to irregular shape of
159   the struts (Figure 4a). Secondly, analysis of the scanning strategy showed that designed fine
160   structures (less than 300 µm) were scanned by the laser as single lines with process-parameters for
161   the skin (contouring). Thus, struts in each of the produced sets of 0.6-1.2 mm units, were similar and
162   had thickness of 90-220 µm and they were very rough (Figure 4b). For the total density, the result is
163   that the larger lattice has larger pore spaces making its actual density lower than designed as shown
164   in Figure 3(b).
165

166   (a)

167   (b)
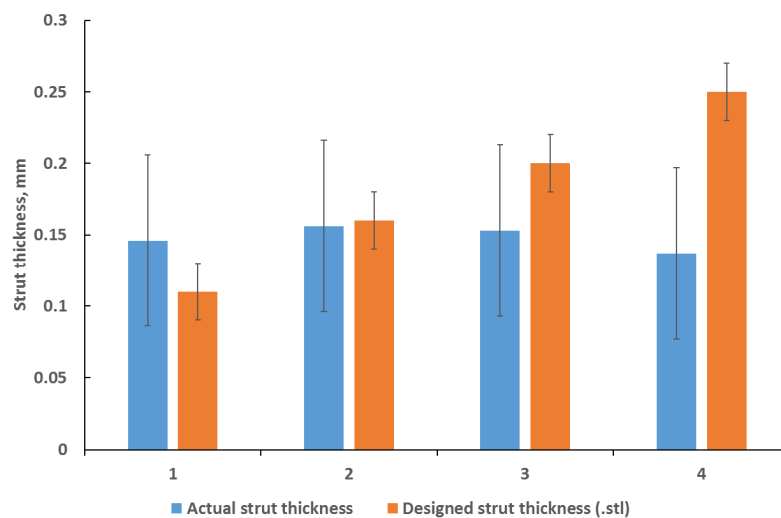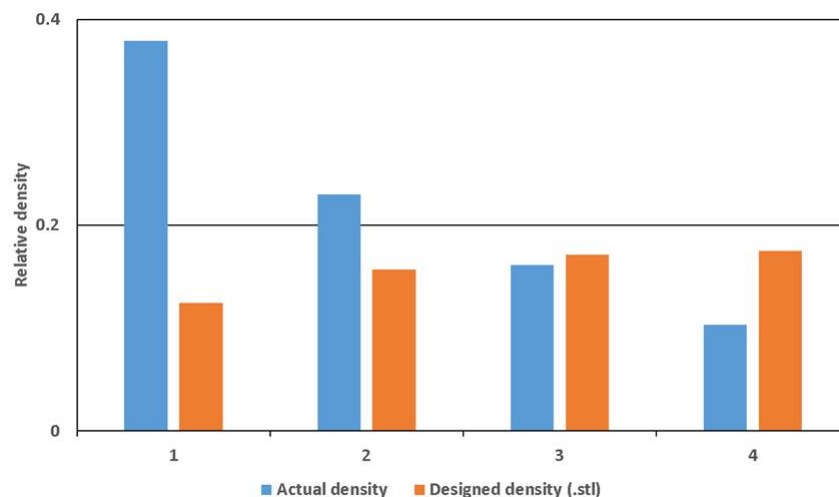
168   **Figure 3.** Dimensional assessment of (a) actual versus designed strut thickness and (b) actual versus
169   designed total density compared to the designed values. Maximum and minimum values are shown
170   as an error margin but indicates the variability within a single strut, as measured manually from 3D
171   model .stl data and microCT data.

172

(a)

173

(b)
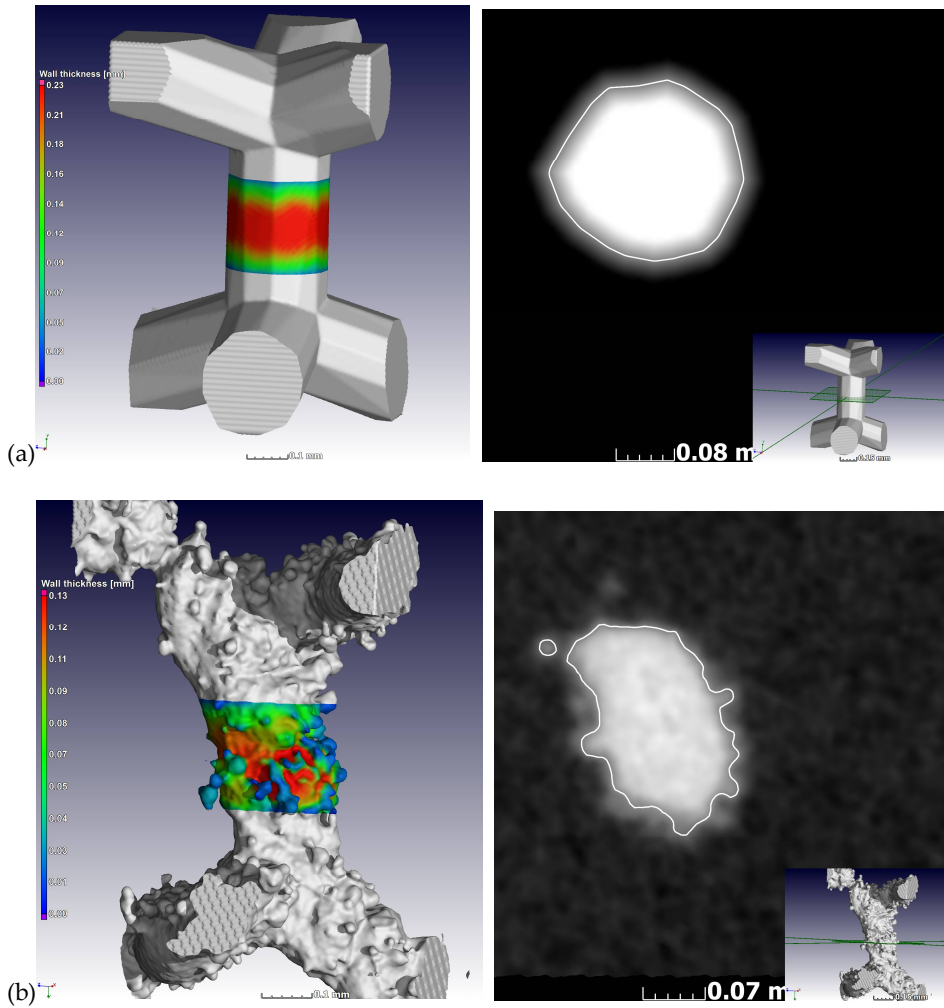
Figure 4. MicroCT voxel view of (a) designed and (b) manufactured struts and their cross-sections,
indicating the actual morphology in each case.

176
177   As explained in the previous section, the simplified model of Ashby-Gibson for open cell foams
178   indicates a linear correlation between the elastic modulus and the square of the density. This is found
179   experimentally in this case with a slope of approximately 2.8 as shown in Figure 5.
180
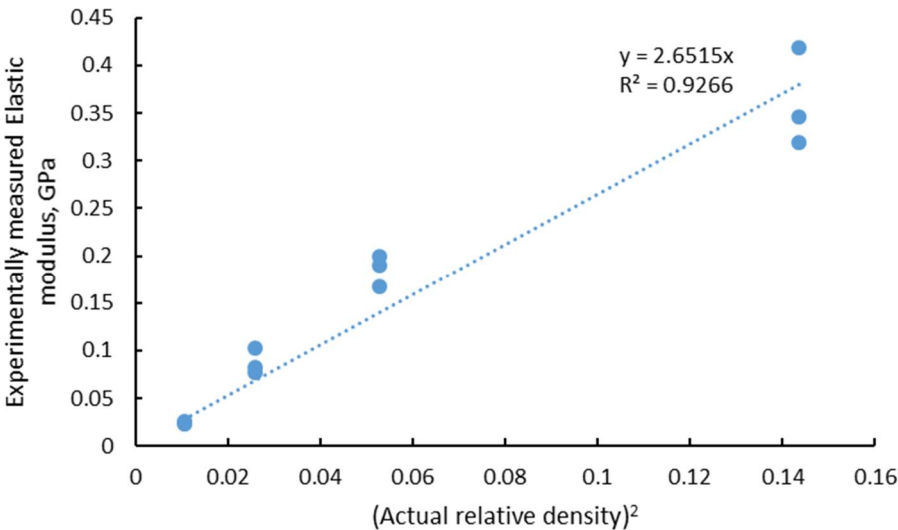
Figure 5. Relationship for experimentally measured elastic modulus and squared relative density of the manufactured LPBF lattices.

The value of 2.8 for the slope is within the expected range of 0.1 – 4. Previous work with larger lattices built using the same material process parameters showed that the experimental elastic modulus values were 10 and 20 GPa for 50% density lattice structures of two designs: diagonal and rhombic [17]. This relates to values for alpha (the slope) of 0.35 to 0.7. We can therefore speculate that as the strut thickness reduces, the effect of the rough and irregular surface plays an increasingly important role increasing the slope and making the structure's mechanical properties more sensitive to changes in density. What is interesting to note here is that since the lattice properties follow the density, the smallest lattice of 3.6 mm (unit cell of 0.6 mm) was the strongest – the yield strength is shown in Table 1 together with the actual relative porosity as measured by microCT. This is due to the similar strut thickness of the 4 models but shorter strut lengths and hence higher density, for the smallest model. This also shows that at this scale the strength and elastic modulus is strongly correlated with the actual porosity (or density).

Table 1. Experimental data.

Unit cell design (mm).	Actual relative porosity (%)	Compressive elastic modulus (MPa)	Compressive strength (MPa)	Maximum load (N)
0.6	63	346 418 318	51.1 54.8 53.4	662 710 692
0.8	77	190 167 200	9.1 9.9 10.1	209 227 232
1.0	84	83 77 102	3.3 3.9 3.6	117 139 130
1.2	90	26 25	1.0 0.9	53 46

		24	1.1	56

197

198

199   In-situ compression allowed imaging of the same lattice prior to full densification – first before
200   loading, then directly after initial yielding, and at a few more representative steps during yielding.
201   This is shown in Figure 6, where red arrows indicate the positions where the loading was stopped
202   and microCT scans were performed. The resulting microCT data is represented for the aligned
203   volumes, with side-by-side slice images through the middle of the lattice, and with 3D views of the
204   entire lattice. These images indicate that yielding occurs gradually and progressively as struts
205   collapse in this type of lattice.

206   (a)

207   (b)

208   (c)
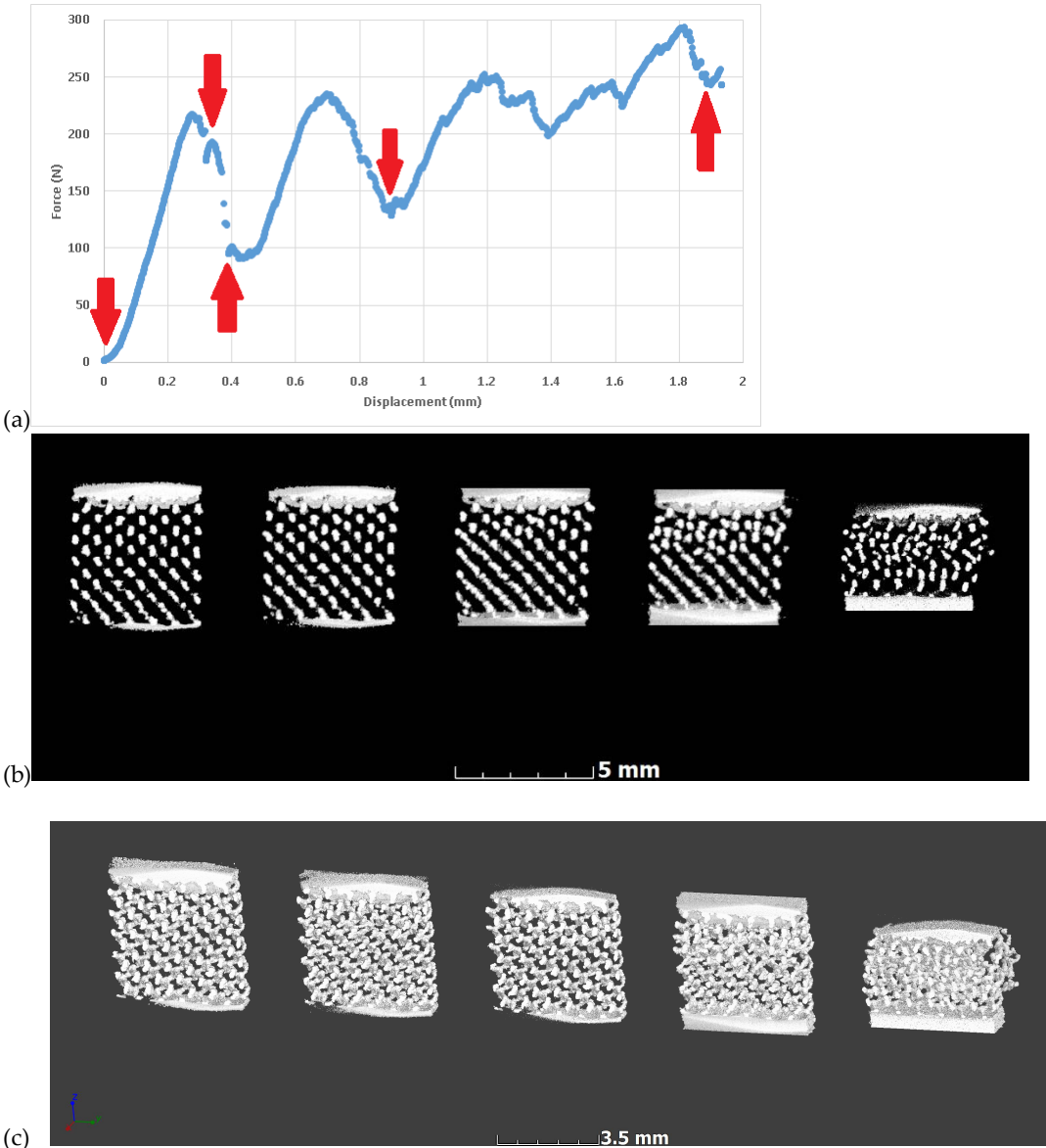
209   .**Figure 6.** In situ deformation imaging of a lattice (0.8 mm unit cell) at the selected points during
210   yielding – steps according to arrows in force-displacement curve. (a) shows force-displacement with
211   red arrows indicating steps for microCT scans (stop), (b) microCT slice images at each step showing
212   collapse and (c) the corresponding microCT 3D images of lattice at each step (cropped).

213

214   The alignment of the scans is simplified by the fact that the sample stays in the same location in
215   the scan system, and as the load cell works by moving the bottom upwards, the deformation can be
216   imaged more closely on individual struts by making the unloaded scan transparent and visualizing

217 the loaded image. This is done in Figure 7 for a small section (approx. 0.5 mm) to visualize the
218 deformation and collapse of individual struts, in this case taken from the middle (away from the edge
219 of the lattice) near the top of the sample, where collapse first occurred.   The light blue transparent
220 struts shown in Figure 7 show the unloaded sample while the third scan in the series is shown here
221 in solid rendering (this is at the first yield dip – the third arrow in Figure 6). The colour coding applied
222 to the loaded sample image is a nominal-actual comparison - this quantitatively shows the
223 deformation value (in red is where largest deformation is relative to the unloaded sample). Besides
224 collapse, the largest deformations occur at the strut junctions. Similar results were reported for
225 Ti6Al4V lattices in [24] where digital image correlation (of external surface of lattice) was used during
226 compression testing of diamond-type lattices. It was found that fracture occurs exclusively at the
227 nodes in this design, and similar layered collapse was observed. The three images are the same region
228 from different viewing angles.

229

230
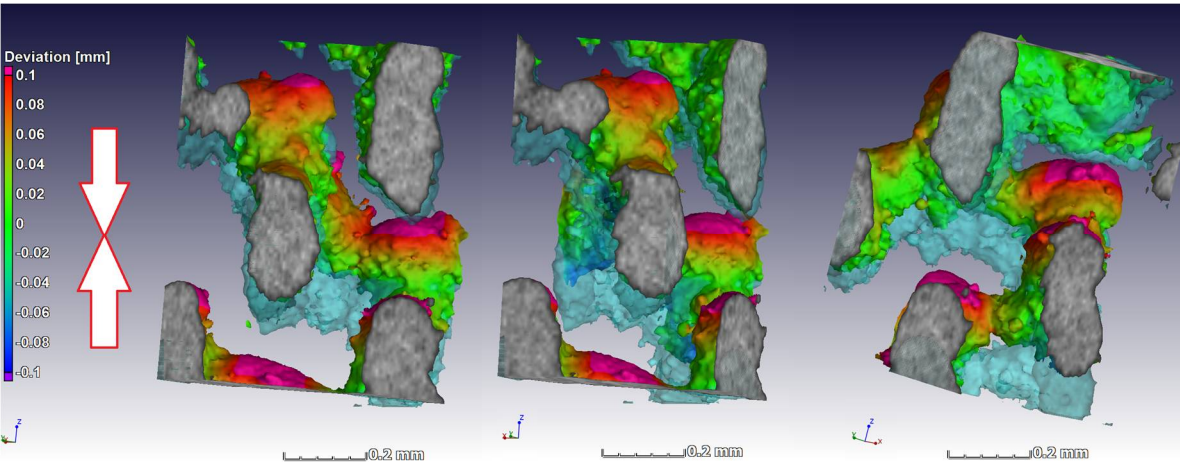
231   **Figure 7.** Three different angular views of the same internal location showing yielding behavior of
232   individual struts and colour coding indicating largest deformation relative to unloaded state
233   (deformation upwards in image, unloaded state semi-transparent blue). Loading direction indicated
234   by arrows.

235

4. Conclusions

237   This paper reported the mechanical properties of a series of micro-lattices with struts near the
238 single track width of the laser powder bed fusion system used to produce them. The results show
239 that such lattices can be produced successfully but the small strut thickness deviates from the
240 designed value. It was shown that, in the limited range investigated here, the mechanical properties
241 of micro lattices produced by LBPF are strongly dependent on actual density and can therefore be
242 predicted with some confidence using this measure alone. Compared to larger lattices, the
243 dependence of the mechanical properties is stronger with density (higher slope in the Ashby-Gibson
244 equation). In-situ microCT imaging demonstrated that the largest deformations under compression
245 occurred at the strut junctions. These images represent the first in-situ images of a full micro-lattice
246 structure's yielding behavior.

247

248 **Author Contributions:** Conceptualization, AdP; Methodology, AdP, IY1,IY2; Software, AdP; Validation,
249 AdP,DK; Formal Analysis, All; Investigation, AdP; Resources, All; Data Curation, All; Writing-Original Draft
250 Preparation, AdP; Writing-Review & Editing, All; Visualization, All.

251 **Funding:** The authors thank the South African Research Chairs Initiative of the Department of Science and
252 Technology and National Research Foundation of South Africa (Grant No. 97994), the Collaborative Program in
253 Additive Manufacturing (Contract No. CSIR-NLC-CPAM-15-MOA-CUT-01).

Peer-reviewed version available at *Materials* **2018**, *11*, 1663; doi:10.3390/ma11091663

254   **Conflicts of Interest:** The authors declare no conflict of interest.

255   **References**

256   1. M. Schmidt et al., "Laser based additive manufacturing in industry and academia," CIRP Ann., vol. 66, no.
257   2, pp. 561–583, Jan. 2017.
258   2. T. Debroy et al., "Additive manufacturing of metallic components – Process, structure and properties,"
259   2017.
260   3. I. Yadroitsev, A. Gusarov, I. Yadroitsava, and I. Smurov, "Single track formation in selective laser melting
261   of metal powders," J. Mater. Process. Technol., vol. 210, no. 12, pp. 1624–1631, Sep. 2010.
262   4. A. du Plessis, I. Yadroitsev, I. Yadroitsava, and S. le Roux, "X-ray micro computed tomography in additive
263   manufacturing: a review of the current technology and applications," 3D Print. Addit. Manuf., vol. In press,
264   2018.
265   5. I. Yadroitsev, P. Krakhmalev, I. Yadroitsava, and A. du Plessis, "Qualification of Ti6Al4V ELI Alloy
266   Produced by Laser Powder Bed Fusion for Biomedical Applications," JOM, 2018.
267   6. X. P. Tan, Y. J. Tan, C. S. L. Chow, S. B. Tor, and W. Y. Yeong, "Metallic powder-bed based 3D printing of
268   cellular scaffolds for orthopaedic implants: A state-of-the-art review on manufacturing, topological design,
269   mechanical properties and biocompatibility," Mater. Sci. Eng. C, vol. 76, pp. 1328–1343, Jul. 2017.
270   7. X.-Y. Zhang, G. Fang, and J. Zhou, "Additively Manufactured Scaffolds for Bone Tissue Engineering and
271   the Prediction of their Mechanical Behavior: A Review," Materials (Basel)., vol. 10, no. 1, p. 50, Jan. 2017.
272   8. G. Dong, Y. Tang, and Y. F. Zhao, "A Survey of Modeling of Lattice Structures Fabricated by Additive
273   Manufacturing," J. Mech. Des., vol. 139, no. 10, p. 100906, Aug. 2017.
274   9. L. Gibson and M. Ashby, "Cellular solids: structure and properties," 1999.
275   10. M. Ashby, T. Evans, N. Fleck, and J. Hutchinson, Metal foams: a design guide. 2000.
276   11. J. Parthasarathy, B. Starly, S. Raman, and A. Christensen, "Mechanical evaluation of porous titanium
277   (Ti6Al4V) structures with electron beam melting (EBM)," J. Mech. Behav. Biomed. Mater., vol. 3, no. 3, pp.
278   249–259, Apr. 2010.
279   12. E. Sallica-Leva, A. L. Jardini, and J. B. Fogagnolo, "Microstructure and mechanical behavior of porous Ti–
280   6Al–4V parts obtained by selective laser melting," J. Mech. Behav. Biomed. Mater., vol. 26, pp. 98–108, Oct.
281   2013.
282   13. S. M. Ahmadi et al., "Mechanical behavior of regular open-cell porous biomaterials made of diamond lattice
283   unit cells," J. Mech. Behav. Biomed. Mater., vol. 34, pp. 106–115, Jun. 2014.
284   14. S. Ahmadi et al., "Additively Manufactured Open-Cell Porous Biomaterials Made from Six Different Space-
285   Filling Unit Cells: The Mechanical and Morphological Properties," Materials (Basel)., vol. 8, no. 4, pp. 1871–
286   1896, Apr. 2015.
287   15. F. S. L. Bobbert et al., "Additively manufactured metallic porous biomaterials based on minimal surfaces:
288   A unique combination of topological, mechanical, and mass transport properties," Acta Biomater., vol. 53,
289   pp. 572–584, Apr. 2017.
290   16. A. du Plessis, I. Yadroitsava, I. Yadroitsev, S. le Roux, and D. Blaine, "Numerical comparison of lattice unit
291   cell designs for medical implants by additive manufacturing," Virtual Phys. Prototyp., pp. 1–16, Jun. 2018.
292   17. A. du Plessis, I. Yadroitsava, and I. Yadroitsev, "Ti6Al4V lightweight lattice structures manufactured by
293   laser powder bed fusion for load-bearing applications," Opt. Laser Technol., vol. In press, 2018.
294   18. H. D. Carlton et al., "Mapping local deformation behavior in single cell metal lattice structures," Acta
295   Mater., vol. 129, pp. 239–250, May 2017.
296   19. https://www.materialise.com/en/software/magics. Accessed 12 August 2018
297   20. A. du Plessis, S. G. le Roux, and A. Guelpa, "The CT Scanner Facility at Stellenbosch University: An open
298   access X-ray computed tomography laboratory," Nucl. Instruments Methods Phys. Res. Sect. B Beam
299   Interact. with Mater. Atoms, vol. 384, 2016.
300   21. https://www.volumegraphics.com/en/products/vgstudio-max.html. Accessed 12 August 2018
301   22. D. Kouprianoff, A. du Plessis, I. Yadroitsava, I. Yadroitsev. Destructive and nondestructive testing on small
302   and intricate SLM components. In Proc. RAPDASA 18th International Conference, Durban, Inkosi Albert
303   Luthuli International Convention Centre, November 8- 10, 2017
304   23. Yadroitsava I., Els J., Booysen G., Yadroitsev I., 2015. Peculiarities of single track formation from TI6AL4V
305   alloy at different laser power densities by SLM. The South African Journal of Industrial Engineering, 26 (3):
306   86-95.

307   24.   Liu F, Zhang DZ, Zhang P, Zhao M, Jafar S. Mechanical Properties of Optimized Diamond Lattice Structure
308   for Bone Scaffolds Fabricated via Selective Laser Melting. Materials. 2018;11(3):374.
309   doi:10.3390/ma11030374.
310
311